

## Article

# Effect of Ultrasonic Nanocrystalline Surface Modification (UNSM) on Stress Corrosion Cracking of 304L Stainless Steel

Hyunhak Cho <sup>1</sup>, Young-Ran Yoo <sup>2</sup>  and Young-Sik Kim <sup>1,2,\*</sup> 

<sup>1</sup> Department of Materials Science and Engineering, Andong National University, 1375 Gyeongdong-ro, Andong 36729, Republic of Korea; 20215244@student.anu.ac.kr

<sup>2</sup> Materials Research Centre for Energy and Clean Technology, Andong National University, 1375 Gyeongdong-ro, Andong 36729, Republic of Korea; yryoo@anu.ac.kr

\* Correspondence: yikim@anu.ac.kr; Tel.: +82-54-820-5504

**Abstract:** The nuclear industry uses 304L stainless steel to construct canisters for storing spent nuclear fuel. The spent nuclear fuel canisters require the lifetime prediction and robustness of their corrosion behavior over periods ranging from thousands to hundreds of thousands of years. Since nuclear power plants are predominantly located in coastal areas, where storage conditions are highly vulnerable to chloride environments, extensive research has been conducted to enhance the canisters' stress corrosion cracking (SCC) resistance. The welded canisters inherently possess residual tensile stress, prompting the application of plastic deformation-based techniques to boost their SCC resistance, with peening being the most prevalent method. It is reported that UNSM increases the SCC resistance by plastic deformation through surface treatment. In this study, the commercial 304L stainless steel was subjected to UNSM treatment on base metal, heat affected zone (HAZ), and weld metal U-bend test specimens to induce compressive residual stresses up to a depth of 1 mm. The impact of peening treatment on SCC properties was explored through microstructural analysis, corrosion properties analysis, and compressive residual stress assessments. The U-bend specimens underwent SCC testing (in 42% MgCl<sub>2</sub> at 155 °C), microstructure examination using an optical microscope (OM) and a scanning electron microscope (SEM), electron backscatter diffraction (EBSD) analysis, and compressive residual stress measurements via the hole-drilling method. Corrosion behavior on the surface and cross-section was evaluated using anodic polarization tests, electrochemical impedance spectroscopy (EIS) measurements, double loop-electrochemical potentiokinetic reactivation (DL-EPR) tests, and ASTM A262 Pr. C tests. The compressive residual stress imparted by UNSM refined the outermost grains of the cross-section and enhanced the corrosion resistance of 304L stainless steel. Furthermore, it led to a longer crack initiation time, a reduced crack propagation rate, and improved SCC properties.

**Keywords:** stainless steel; welding; UNSM; stress corrosion cracking; residual stress



**Citation:** Cho, H.; Yoo, Y.-R.; Kim, Y.-S. Effect of Ultrasonic Nanocrystalline Surface Modification (UNSM) on Stress Corrosion Cracking of 304L Stainless Steel. *Metals* **2024**, *14*, 1315. <https://doi.org/10.3390/met14121315>

Academic Editor: Petros E. Tsakiridis

Received: 16 October 2024

Revised: 18 November 2024

Accepted: 18 November 2024

Published: 21 November 2024



**Copyright:** © 2024 by the authors. Licensee MDPI, Basel, Switzerland. This article is an open access article distributed under the terms and conditions of the Creative Commons Attribution (CC BY) license (<https://creativecommons.org/licenses/by/4.0/>).

## 1. Introduction

Austenitic stainless steel is employed in the nuclear industry to fabricate canisters for spent nuclear fuel storage. The selection of 304L stainless steel for these canisters is due to its excellent corrosion resistance, good mechanical properties, and weldability [1,2]. However, welded canisters are prone to stress corrosion cracking (SCC) when exposed to chloride environments [3]. The chloride environment and the tensile residual stress generated during welding are the primary causes of SCC [4]. The spent nuclear fuel canister requires the lifetime prediction and robustness of their corrosion behavior over periods ranging from thousands to hundreds of thousands of years [5]. Because nuclear power plants are predominantly located in coastal areas, the austenitic stainless steel is vulnerable to chloride environments, prompting extensive research to enhance its SCC resistance by managing its tensile residual stress in welds for use in nuclear fuel storage canisters [1].

The welding process introduces residual tensile stresses in the structure due to the cooling and solidification processes, leading to defects including microstructural changes; thus, post-treatment methods are applied to manage these issues. To minimize defects in welded structures and enhance SCC resistance, techniques based on plastic deformation are commonly used, with plastic deformation typically induced through physical collisions or shock waves [1,6]. Among these plastic modification methods, peening techniques are extensively utilized, including shot peening (SP) [7,8], laser shock peening (LSP) [9–11], water jet peening (WJP) [12,13], ultrasonic shot peening (USP) [14–17], and ultrasonic nanocrystal surface modification [18–22]. Surface modification treatments can plastically deform the material's surface to refine the grain, convert tensile residual stresses to compressive ones, and enhance surface properties [23–25]. These technologies are known to plastically deform the surface of the material, to add a compressive residual stress to the surface, and to refine the surface grains. It has also been reported that grain refinement can inhibit the surface corrosion by reducing the interatomic distance, promoting interatomic diffusion, and maintaining a passive film [4,26]. However, it must be considered that peening can also roughen the material's surface, potentially serving as a corrosion initiation site if uneven or overlaps are present [2,23].

We recently evaluated the impact of LSP and USP on improving the SCC properties of 304L stainless steel and made the following observations: LSP induced compressive residual stresses on the surface of 304L stainless steel, decreasing both the gross and net crack propagation rates in the U-bend test [4]. Additionally, the SCC characteristics were enhanced by USP due to the refined grains on the surface, which delayed crack initiation and reduced the crack growth rate [6]. Conversely, the pitting and intergranular corrosion properties of the peened surface showed a weak correlation with the SCC properties [4,6].

UNSM employs ultrasonic vibrational energy to repeatedly strike a ball against a metal surface with high static and dynamic forces, over 20,000 times per second (approximately 1000 to 100,000 times/mm<sup>2</sup>) [22]. This process causes severe plastic deformation (SPD) and elastic deformation, transforming the microstructure of the surface layer into nanocrystals [19,22]. Moreover, nanostructuring the metal surface enhances its hardness and imparts compressive residual stress [22,27]. UNSM comprises a vibrator (20 or 40 kHz), a booster, and a horn, as described in the literature; it exhibits a machining pattern with a ball tip at the horn's end to secure the ball [19,22,28,29]. The material surface adopts a dimpled pattern and achieves a lower surface roughness compared to a polished surface [19,22,28].

According to the literature, the application of UNSM refines the grains on the outermost surface of the sample and increases the Cr content to enhance the pitting resistance and prevent MnS formation [18]. However, compressive residual stresses on the surface can induce deformation-induced martensitic transformation, thereby reducing the corrosion resistance [18]. Studies on the effect of UNSM treatment on the SCC of AISI 316L showed that it hardens the surface, raises the likelihood of sharp crack nucleation, and leads to transgranular SCC failure mode [30]. Additionally, J. H. Lee and colleagues investigated the impact of UNSM treatment on the intergranular corrosion of AISI 316L at 650 °C, finding that the compressive stress from the UNSM treatment enhances the resistance to intergranular corrosion by preventing carbon segregation on the top surface through grain refinement [31]. Ling and Ma and others found a hard layer on the top surface with ultra-fine grains following ultrasonic peening on gas tungsten arc welding (GTAW), thus concluding that welded 304 stainless steel improves SCC resistance [32]. The materials corresponding to austenitic stainless steel are subdivided due to planar dislocations, intersections of twins, and multidirectional twins. This causes strain-induced martensitic transformation responsible for refining and forming nanocrystals. The refined microstructure significantly enhances the chemical activity of the surface due to increased grain boundaries, which aids in the robustness and reliability of the passive film [19]. These studies reported that compressive residual stress and microstructural changes due to plastic deformation play a crucial role in enhancing SCC resistance [19].

As previously discussed, for use in spent fuel storage canisters, 304L stainless steel must counteract the vulnerability of welds to SCC. UNSM, as an applied technology, improves SCC resistance by inducing plastic deformation through surface treatment. In this study, UNSM treatment was applied to 304L stainless steel welds, and the peened specimens were subjected to compressive residual stress up to a depth of 1 mm from the surface. The main factors and causes affecting the SCC properties after such peening treatments were examined from the perspectives of microstructure, corrosion properties, and compressive residual stress.

## 2. Experimental Methods

### 2.1. Specimen

In this study, commercial 304L was used as the base metal, and the specimens were welded by GTAW process [2]. The base metal was designated as 304LB, and the welded metal was designated as 304LW [2]. Table 1 shows the chemical composition of the base metal 304L and the filler metal ER308L used in the experiments, which meet the specifications. The thickness of the base metal used for GTAW welding was 25 mm, and the groove angle was machined to 15° and used for welding. Table 2 details the welding conditions, including welding current, voltage, welding speed, and shielding gas. Table 3 summarizes the specimens, including base metal, heat-affected zone, and weldment. Many variables were considered in this study.

**Table 1.** Chemical composition of 304L stainless steel and filler metal (wt %).

Composition	C	Cr	Ni	Mn	Si	Cu	Mo	Co	P	N	S	Cb + Ta	Fe	
304L	0.02	18.6	9.6	1.7	0.47	-	-	0.03	0.02	0.07	0.03	-	Bal.	
ER308L	Spec.	≤0.03	19.5–22.0	9.0–11.0	1.0–2.5	0.30–0.65	≤0.75	≤0.75	-	≤0.03	-	≤0.03	-	Bal.
	analysis	0.02	19.8	9.8	1.7	0.35	0.12	0.05	0.03	0.02	0.04	0.03	0.01	Bal.

**Table 2.** Welding conditions of the experimental specimen (adapted from Ref. [2]).

Welding Process	Current (A)	Voltage (V)	Speed (cm/min.)	Shield Gas (%)	Groove Angle (°)	Welding Electrode
GTAW	240–250	14–15	9–10	Ar. 99.9	15	ER308L (Dia. 0.9 mm wire)

**Table 3.** Designation of the experimental specimen.

	Alloy	Non-Peened	UNSM-Treated
304L	Base metal	304LB	304LB-UNSM
	HAZ area	304LW-H	304LW-H-UNSM
	Weldment	304LW-W	304LW-W-UNSM

### 2.2. Ultrasonic Nanocrystal Surface Modification Treatment

As shown in Table 4, the UNSM induces large compressive residual stresses on material surface by transferring power generated from the generator to a tungsten carbide indenter located at the end of the UNSM unit head at 20 kHz frequency and causing the indenter to repetitively impact the material [23].

**Table 4.** Ultrasonic nanocrystal surface modification processing conditions.

Specimen Type	Frequency (kHz)	Ultrasonic Generator Output (%)	Static Load (N)	Velocity (mm/min)	Interval (mm)	Indenter Material	Indenter Diameter (mm)
Base metal and Welded specimen	20	30	120	2000	0.07	Tungsten Carbide	2.38

### 2.3. Microstructure Analysis

Specimens for microstructural observation were cut to  $15 \times 15 \times 10$  mm and polished using #2000 SiC paper and  $3 \mu\text{m}$  diamond paste. The polished specimens were etched using an electrolytic etcher (Lectropol-5, Struers, Champigny sur Marne cedex, France) in a 10% oxalic acid solution and cleaned with ethyl alcohol in an ultrasonic cleaner (Branson 3210 Ultrasonic Cleaner, Branson, MO, USA). The cleaned specimens were examined for microstructure using an optical microscope (AXIOTECH 100 HD, ZEISS, Oberkochen, Germany).

The cross-sections of the cracked specimens after the U-bend test were observed by SEM (VEGA II LMU, Tescan, Brno, Czech Republic). Specimens for EBSD (Oxford Instruments, Bognor Regis, UK) analysis were ground with #2000 SiC paper and polished with  $3 \mu\text{m}$  diamond paste (DP-Paste M, Struers, Champigny sur Marne cedex, France). After ion milling (IM 4000, Hitachi, Tokyo, Japan), EBSD was measured using a field emission scanning electron microscope (FE-SEM, MIRA3 XMH, Tescan, Brno, Czech Republic) with an EBSD instrument attached. EBSD analysis was performed with a step size of  $0.3 \mu\text{m}$ .

### 2.4. Corrosion Test

#### 2.4.1. U-Bend SCC Test

U-bend specimens for SCC testing were prepared in accordance with ASTM (d size) G30 [33], and welded specimens were prepared in accordance with ASTM G58 [34].

SCC test was performed according to ASTM G36 [35] in 42%  $\text{MgCl}_2$  test solution at  $155^\circ\text{C}$  boiling temperature. During the test, the U-bend area was observed every 1.5 or 3 h, depending on the specimen, to check for crack initiation. The sides of the U-bend specimens were insulated (high-temperature adhesive) to prevent cracks from developing in the area where the peening was applied [6].

SCC resistance was measured by comparing “crack time” and “crack propagation rate”. In this work, crack time was divided into total crack time, which means the time when cracks were identified by periodic observation during the SCC test, and crack initiation time, which means the last time when cracks were not observed by periodic observation.

The cracks in the cross-section after the SCC test were observed using an OM (AXIOTECH 100HD, ZEISS, Oberkochen, Germany). The cross-section of the specimen was polished with #2000 SiC paper (CC261, DEERFOS, Seoul, Republic of Korea) and then polished with diamond paste ( $3 \mu\text{m}$ ) (DP-Paste M, Struers, Champigny sur Marne cedex, France). To observe the polished surface, the specimens were etched using an electrochemical etcher (Lectropol-5, Struers, Champigny sur Marne cedex, France) in a 10% oxalic acid solution. The surface of the etched specimens was observed using an OM, and the crack length was measured; the crack mode was observed using an SEM (VEGA II LMU, Tescan, Brno, Czech Republic) [4]. The crack propagation rate was calculated from the crack length and crack time [4].

- Total crack propagation rate = crack length/total crack time
- Net crack propagation rate = crack length/(total crack time – crack initiation time)

#### 2.4.2. Electrochemical Test

The specimens, cut to dimensions of  $15 \times 15 \times 10$  mm, were electrically connected for electrochemical testing. An area of  $0.09 \text{ cm}^2$  was left exposed in the specimens, including the non-peened and peened areas, and the rest of the area was coated with epoxy resin.

A potentiostat (Interface 1000, Gamry Instruments, Warminster, PA, USA) was used for electrochemical measurements. The reference electrode was a saturated calomel electrode, and the counter electrode was a Pt wire. The anodic polarization test was performed at  $30^\circ\text{C}$  using a 1% NaCl solution (de-aerated at a rate of  $200 \text{ mL N}_2/\text{min}$  for 30 min.) at a scan rate of  $0.33 \text{ mV/s}$  and a potential 100 mV below the corrosion potential [2]. EIS evaluation was performed in a  $30^\circ\text{C}$ , 1% NaCl solution (de-aerated at a rate of  $200 \text{ mL N}_2/\text{min}$  for 30 min). The tests were performed over a frequency range of 0.01 to 10,000 Hz at the corrosion potential, and the AC voltage amplitude was 10 mV [23].

To detect susceptibility to intergranular attack, the test specimens were aged at 675 °C for 1 h. The DL-EPR test was performed at 30 °C using a mixed solution of 0.5 M H<sub>2</sub>SO<sub>4</sub> and 0.01 M KSCN (de-aerated at a rate of 200 mL N<sub>2</sub>/min for 30 min) and was based on the ASTM G108 standard [36], and a degree of sensitization (DOS) was calculated. The DOS was calculated as the ratio of the reactivation current density (Ir) to the activation current density (Ia) (Ir/Ia) to evaluate the sensitization of the specimen. The intergranular corrosion (IGC) test is a modified ASTM A262 Pr. C test [30] method and was performed by immersion in 65% nitric acid (HNO<sub>3</sub>) at boiling point.

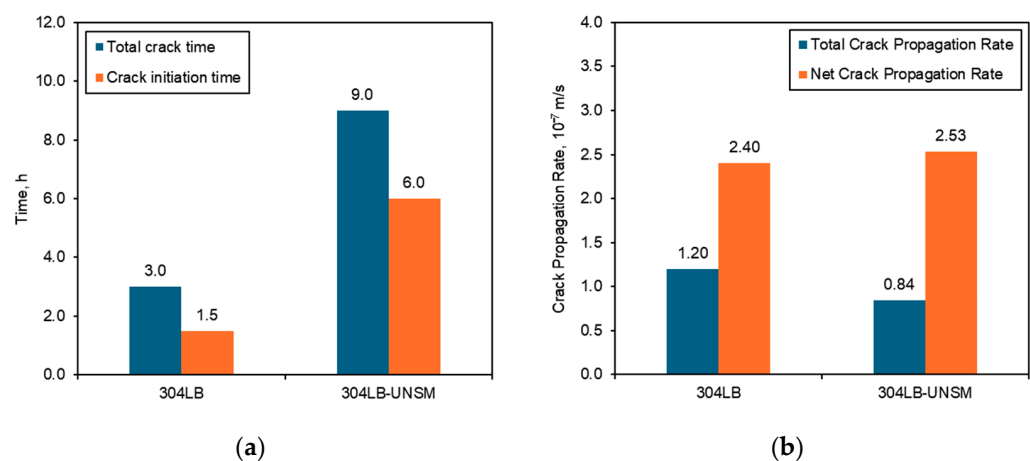
### 2.5. Residual Stress Measurement

The surface residual stress measurement of the specimens was performed using the hole-drilling method (RS-200 Assembly, VMM, Raleigh, NC, USA). A strain gauge (CEA-06-062UL-12, VMM, Raleigh, NC, USA) was attached to the specimen, and a hole was drilled using a drilling device; the residual stresses released during drilling were measured. The residual stresses released in the bending specimen were measured in the apex area of the peened specimen.

## 3. Results

### 3.1. Effect of UNSM on SCC of 304L Stainless Steel and Welded 304L Stainless Steel

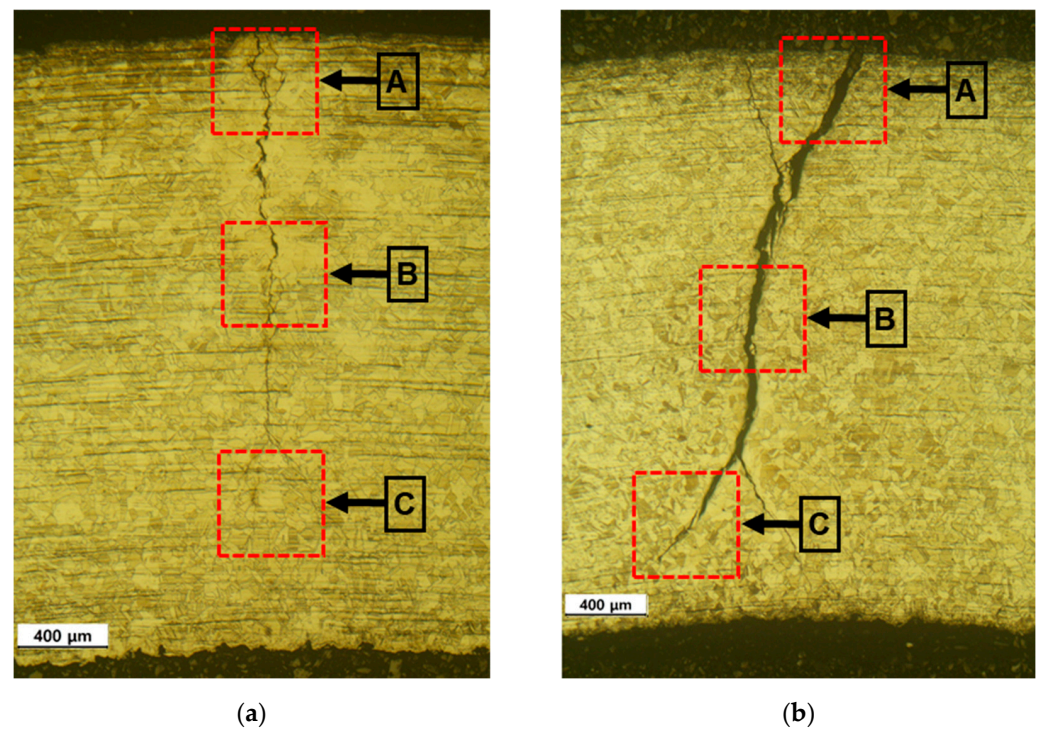
Figure 1 illustrates the SCC test results for the 304L stainless steel U-bend specimens treated with UNSM. Figure 1a indicates that 304LB exhibits a total crack time of 3 h and a crack initiation time of 1.5 h. In contrast, 304LB-UNSM demonstrates a total crack time of 9 h and a crack initiation time of 6 h, with delays attributed to the peening treatment. Figure 1b presents the crack growth rate results, revealing that 304LB has a total crack growth rate of  $1.20 \times 10^{-7}$  m/s and a post-initiation growth rate of  $2.40 \times 10^{-7}$  m/s. After peening, 304LB-UNSM's total crack growth rate reduced to  $0.84 \times 10^{-7}$  m/s, while the growth rate after initiation marginally increased to  $2.53 \times 10^{-7}$  m/s. Both the total and initiation times for cracks increased following the UNSM treatment, while the overall and post-crack growth rates decreased. The delay in crack initiation and growth is likely due to peening, which may cause surface grain refinement [19,30].



**Figure 1.** Impact of UNSM on crack times in U-bended 304LB subjected to SCC testing at 155 °C and 42% MgCl<sub>2</sub>; (a) crack time and (b) crack propagation rates.

Figure 2 depicts a 304L stainless steel base metal with observable cracks post-U-bend test. Figure 2a details the crack observation in the cross-section of a non-peened 304LB specimen (OM,  $\times 50$ , 42% MgCl<sub>2</sub> at 155 °C), showing a mixed crack consisting of both intergranular and transgranular cracks. Figure 2b illustrates the cracks in the cross-section of a 304LB-UNSM specimen (OM,  $\times 50$ , 42% MgCl<sub>2</sub> at 155 °C), also displaying a mixed crack morphology composed of intergranular and transgranular cracks. The 304LB exhibits

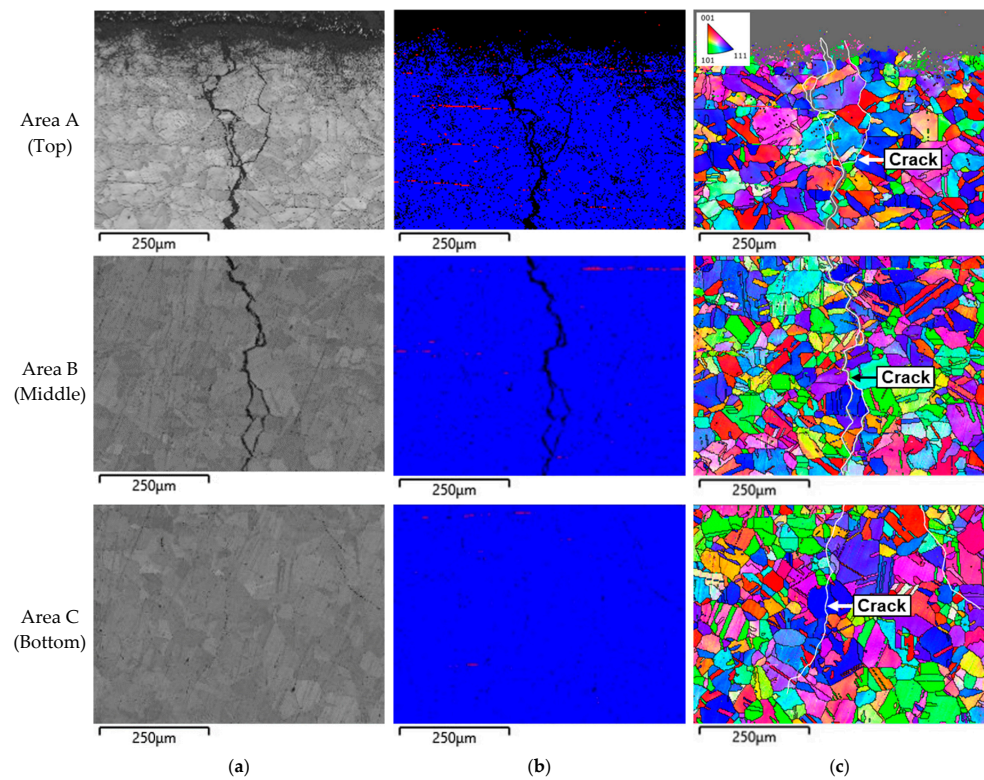
minor differences in crack morphology in U-bend specimens after SCC testing, with and without peening.



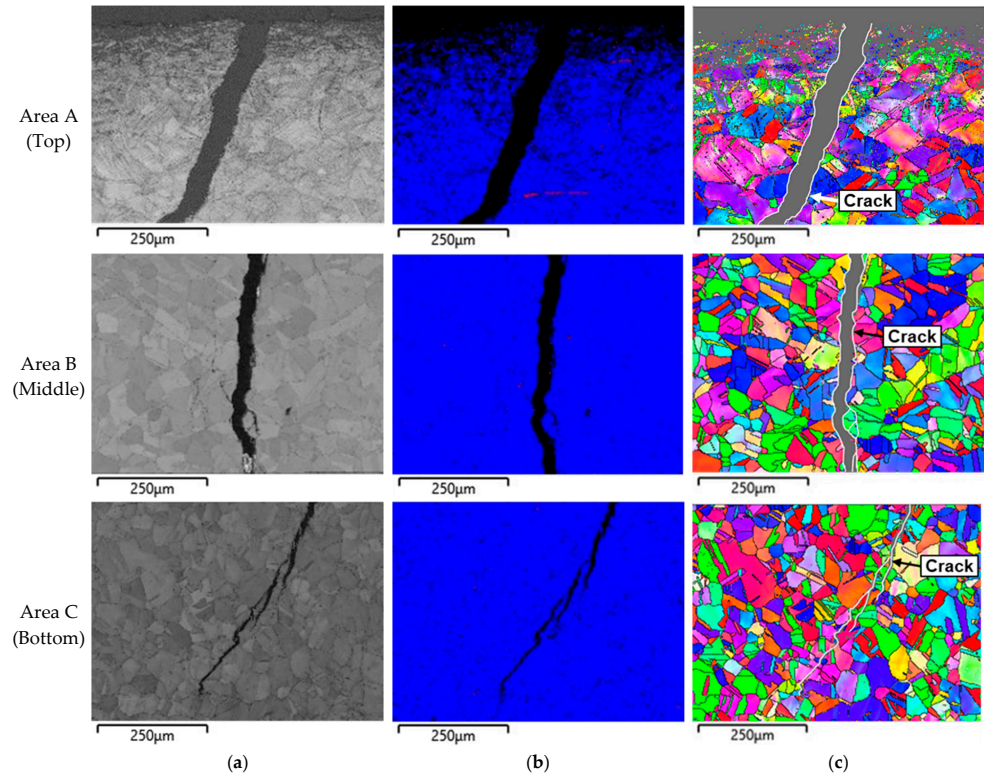
**Figure 2.** Image of the cross-section of U-bended 304LB after SCC test (OM,  $\times 50$ , 42%  $\text{MgCl}_2$  at  $155^\circ\text{C}$ ) (A: top of the crack, B: middle of the crack, C: bottom of the crack); (a) 304LB (Non-peened) and (b) 304LB-UNSM.

Figure 3 shows the EBSD observation of cracks after the U-bend test in 304L stainless steel base material. As depicted, the band contrast analyzes the microstructure of grains, indicating their quality and deformation state. The phase color elucidates the distribution and crystal structure of various phases, while the inverse pole figure (IPF) coloring reveals the orientation of grains along with the properties and deformation behavior of the grain boundaries. Figure 3a,c depicts the non-peened specimen with a flat outermost surface, and Figure 3b exhibits a crack growing perpendicular to the tensile stress. The crack mode was assessed by comparing the lengths of the intergranular and transgranular cracks. The crack propagation in Figure 3c exhibits a mixed crack mode. Conversely, Figure 4a,c demonstrates that peening has refined the grains at the outermost areas of the cross-section, and plastic deformation is observed. However, crack initiation appears not to be significantly influenced by pitting or defects [37,38]. Figure 4b shows the crack propagation path as perpendicular to the direction of tensile stress, and the cracks in Figure 4c display a transgranular mode.

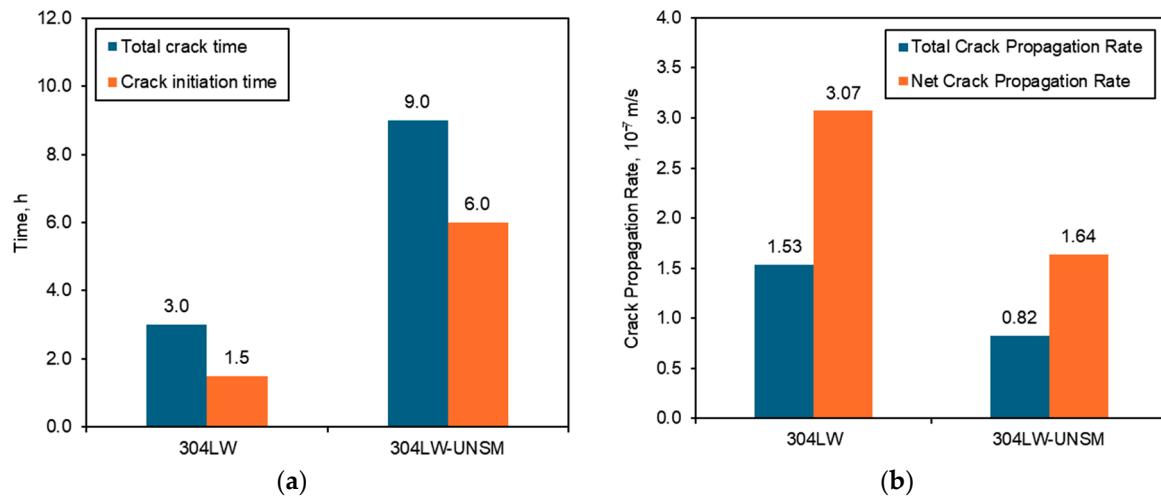
Figure 5 displays the SCC test results of a U-bend specimen of welded 304L stainless steel after UNSM treatment. Figure 5a illustrates that 304LW had a total crack time of 3 h and a crack initiation time of 1.5 h. The 304LW-UNSM exhibited a total crack time of 9 h and a crack initiation time of 6 h, similar to 304LB-UNSM, confirming that the peening treatment delays crack initiation. Figure 5b indicates that the total crack growth rate was  $1.53 \times 10^{-7}$  m/s for 304LW and  $0.72 \times 10^{-7}$  m/s for 304LW-UNSM, while the growth rate post-crack initiation was  $3.07 \times 10^{-7}$  m/s for 304LW and  $2.17 \times 10^{-7}$  m/s for 304LW-UNSM. Like the base metal, the welded metal demonstrated an increase in the total crack time and crack initiation time with UNSM treatment [19,30].



**Figure 3.** EBSD results of the cross-section of 304LB (Non-peened) after SCC test (EBSD: step size  $0.3\ \mu\text{m}$ ); (a) Band contrast, (b) Phase color, and (c) IPF color.

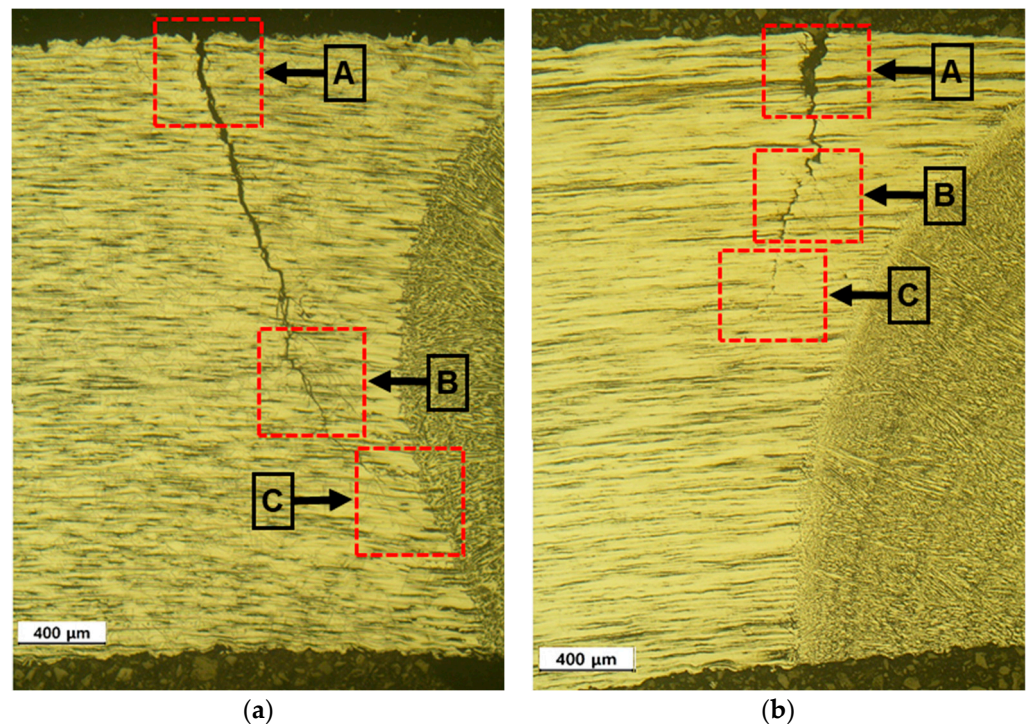


**Figure 4.** EBSD results of the cross-section of 304LB-UNSM after SCC test (EBSD: step size  $0.3\ \mu\text{m}$ ); (a) Band contrast, (b) Phase color, and (c) IPF color.



**Figure 5.** Effect of UNSM on the crack times of U-bended 304LW by SCC test at 155 °C, 42% MgCl<sub>2</sub>; (a) crack time and (b) crack propagation rates.

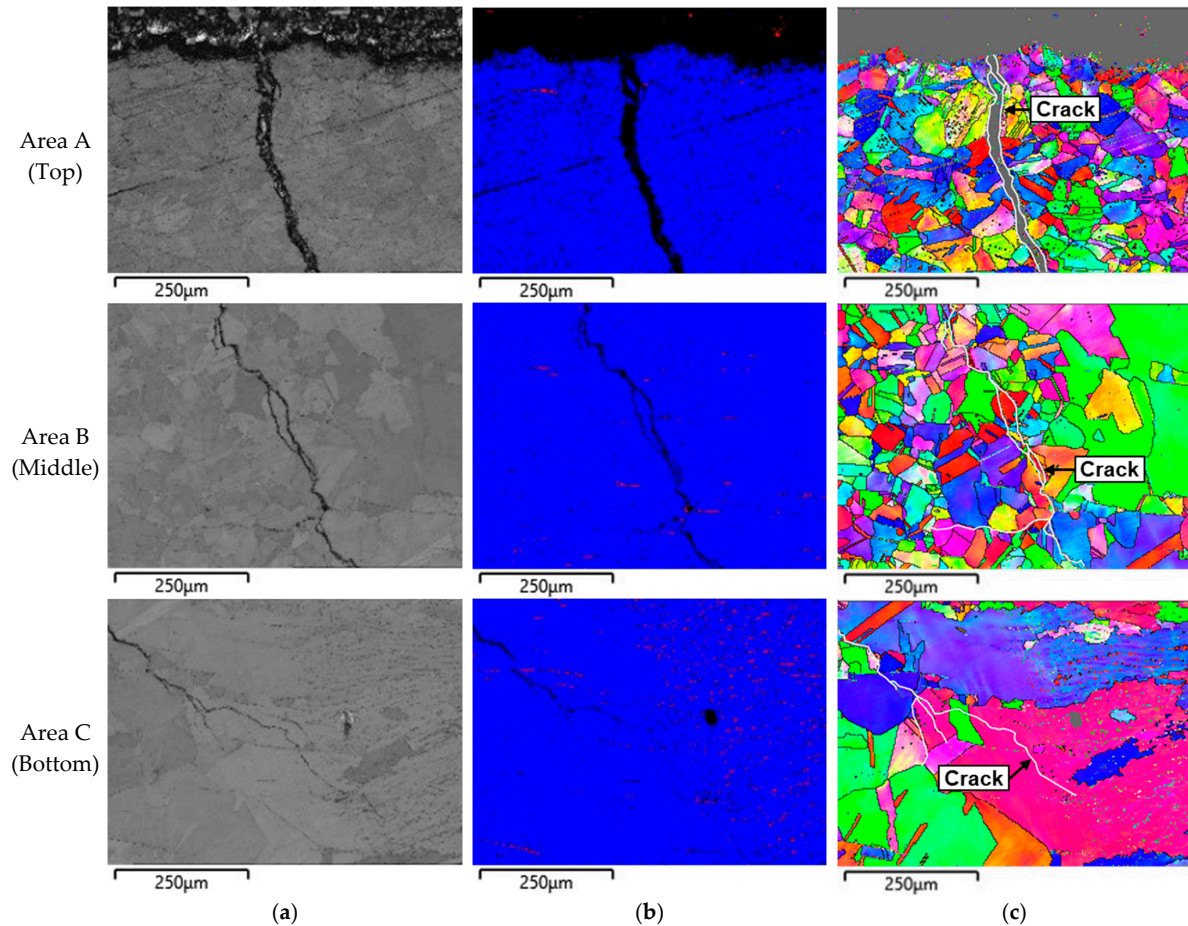
Figure 6 illustrates a 304L stainless steel welded metal with observed cracks after the U-bend test. Figure 6a reveals the crack observation of the non-peened 304LW specimen cross-section (OM,  $\times 50$ , 42% MgCl<sub>2</sub> at 155 °C), and Figure 6b displays the cracks of the 304LB-UNSM specimen cross-section (OM,  $\times 50$ , 42% MgCl<sub>2</sub> at 155 °C), with transgranular cracks noted throughout. A similar crack morphology is exhibited by 304LW in the U-bend specimen post-SCC testing, with and without peening.



**Figure 6.** Image of the cross-section of U-bended 304LW following the SCC test (OM,  $\times 50$ , 42% MgCl<sub>2</sub> at 155 °C) (A: top of the crack, B: middle of the crack, C: bottom of the crack); (a) 304LW (Non-peened) and (b) 304LW-UNSM.

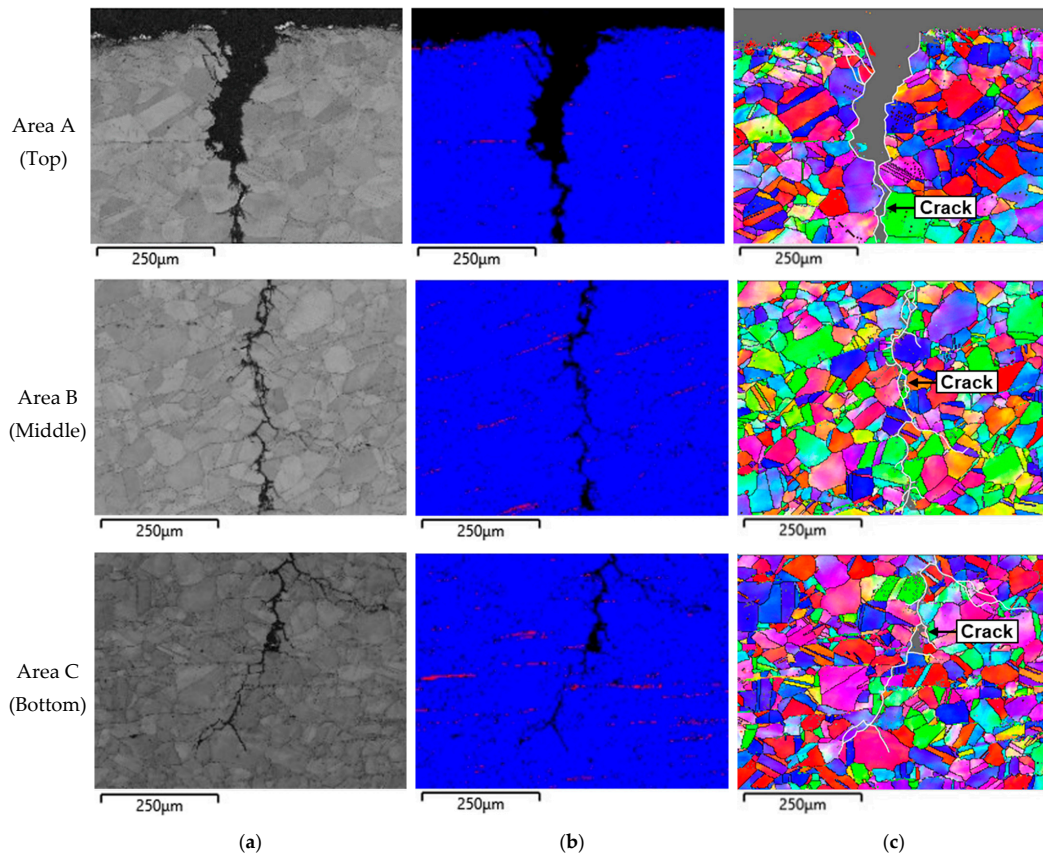
Figure 7 presents the EBSD observation of the crack after the U-bend test of the 304L stainless steel welded metal. Figure 7a,c shows the non-peened specimen, and an uneven surface can be seen in Area A. Figure 7b indicates that the crack grows perpendicular to the tensile stress, and the  $\delta$ -ferrite phase is observed near the weld. The cracks in

Figure 7c exhibit a primarily transgranular mode. Figure 8a,c demonstrates that the peening refined the grains to the outermost areas of the cross-section, extending the zones of grain refinement and plastic deformation near the weld. The cracks in Figure 8c predominantly show a transgranular mode.

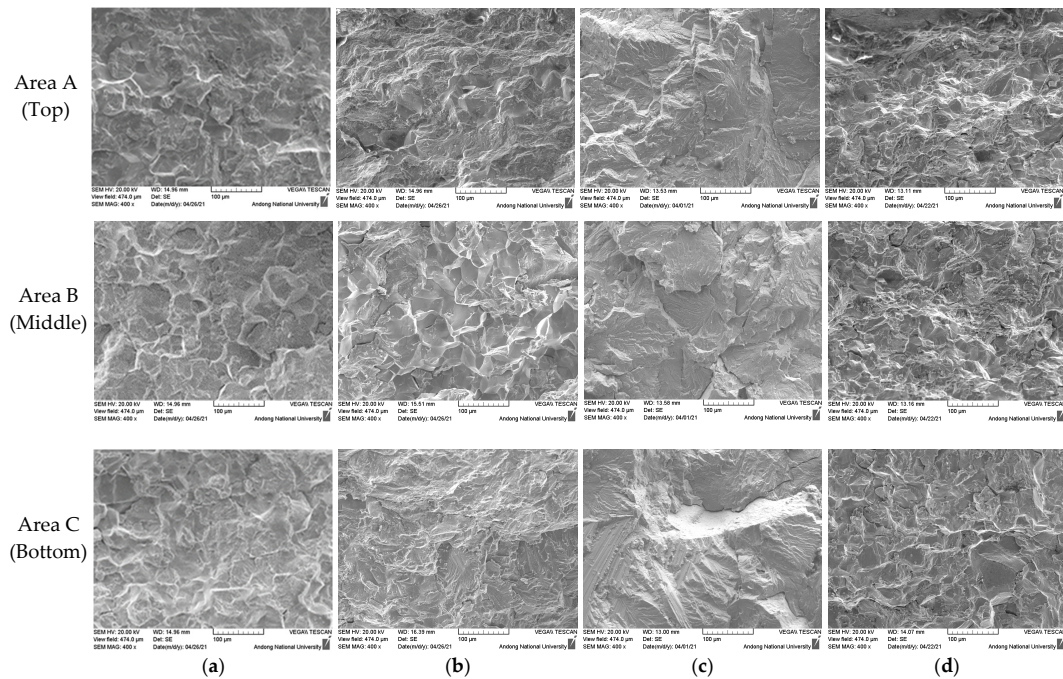


**Figure 7.** EBSD results of the cross-section of 304LW (Non-peened) after SCC test (EBSD: step size 0.3  $\mu\text{m}$ ); (a) Band contrast, (b) Phase color, and (c) IPF color.

Figure 9 illustrates the crack cross-section after a U-bend test on both base metal and welded metal specimens of 304L stainless steel, wherein the crack was observed (SEM,  $\times 400$ ; 42%  $\text{MgCl}_2$  at 155  $^\circ\text{C}$ ; Areas A, B, and C) by fracturing the cracked specimen. The crack mode was discerned by examining the crack cross-section. Figure 9a reveals the 304LB specimen exhibiting a mixed crack morphology comprising both intergranular and transgranular modes, while Figure 9b presents the transgranular crack mode across all sections of the 304LB-UNSM specimen. The 304LB revealed that the crack morphology of the U-bend specimen post-SCC testing varied with and without peening. Figure 9c exhibits the transgranular crack mode in all sections of the 304LW specimen, and Figure 9d shows the same crack mode for the 304LW-UNSM in all observed areas. The 304LW exhibits a consistent crack morphology in the U-bend specimen following SCC testing, both with and without peening.



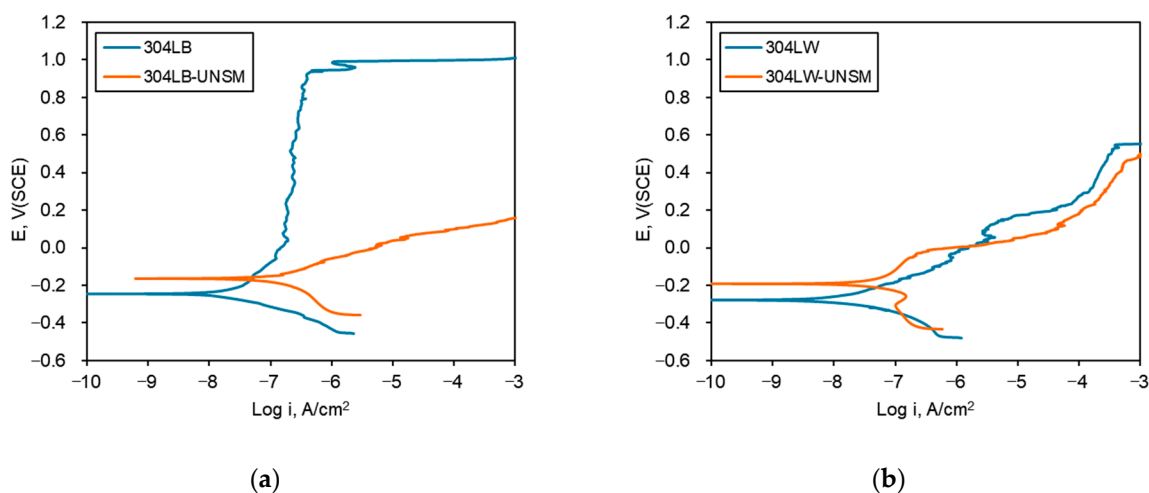
**Figure 8.** EBSD results of the cross-section of 304LW-UNSM after SCC test (EBSD: step size 0.3 µm); (a) Band contrast, (b) Phase color, and (c) IPF color.



**Figure 9.** Crack mode of 304LB and 304LW after the U-bend test (SEM, ×400; 42% MgCl<sub>2</sub> at 155 °C; Areas A, B, and C); (a) 304LB (Non-peened), (b) 304LB-UNSM, (c) 304LW (Non-peened), and (d) 304LW-UNSM.

### 3.2. Impact of UNSM on the Corrosion Properties and Microstructure of the Surface of 304L Stainless Steel

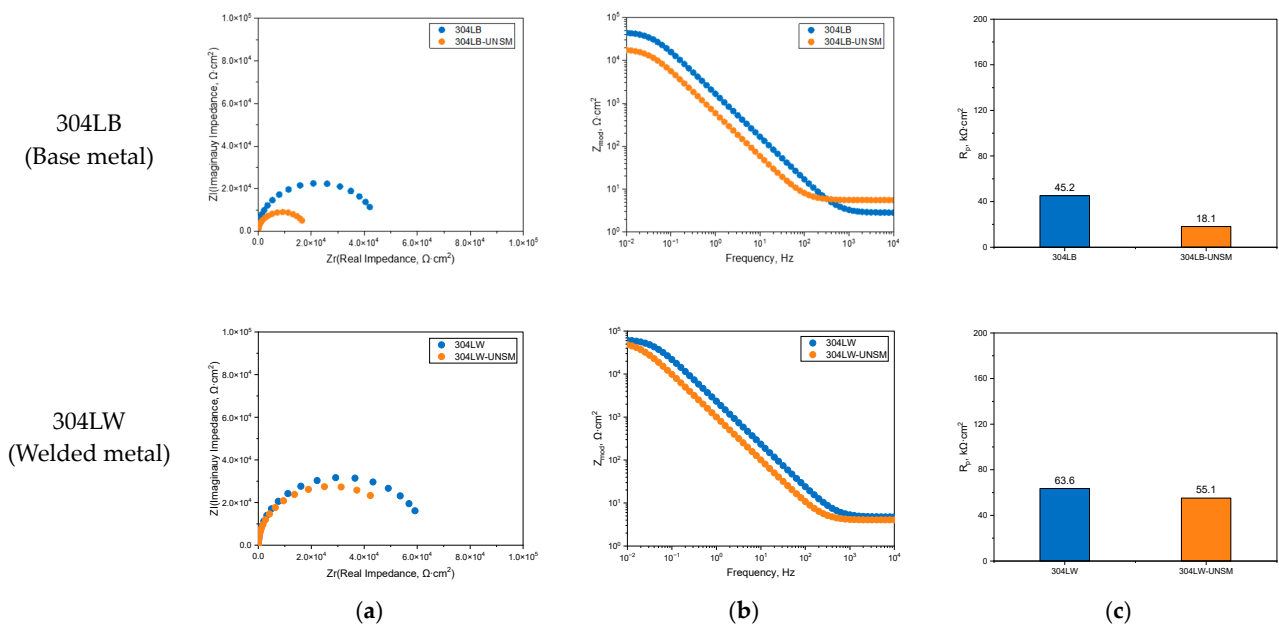
Figure 10 shows the polarization curves of the base and welded metals of 304L stainless steel under de-aerated 1% NaCl at 30 °C following UNSM treatment. Figure 10a presents the polarization curve for 304LB, with a transpassive potential of 935 mV (SCE). Conversely, the peened 304LB-UNSM has deteriorated polarization properties of the surface. Figure 10b reveals that the welded metal, whether peened or not, failed to maintain a stable passivation state. The measured current density at 0 mV (SCE) indicates a slightly lower value for 304LW-UNSM compared to 304LW. The literature suggests that UNSM treatment enhances passivation properties through grain refinement, increased dislocation density, and enhanced surface reactivity [19]. However, UNSM might decrease corrosion resistance in overlapped surface areas, forming crevices that act as pitting initiation sites [23]. As depicted below, the 304LB-UNSM likely experiences reduced corrosion resistance in the overlapped areas due to the amplitude of ultrasonic waves during peening [23].



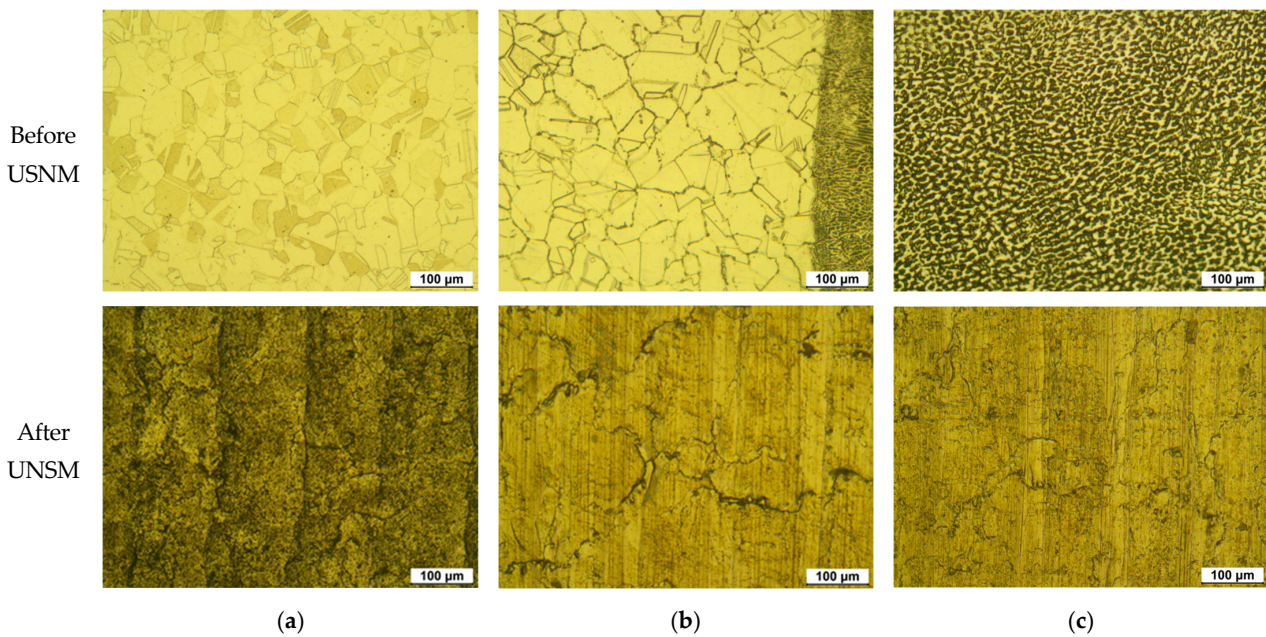
**Figure 10.** Effect of UNSM on the polarization behavior of 304L stainless steel surface in de-aerated 1% NaCl at 30 °C at a scan rate of 0.33 mV/s; (a) 304LB (Base metal) and (b) 304LW (Welded metal).

Figure 11 displays the EIS evaluation results for the surface of the 304L stainless steel base and welded metals after UNSM treatment, calculating polarization resistance ( $R_p$ ) and solution resistance ( $R_s$ ) using an equivalent circuit in the Randles model [39]. The resistance of the passive film is measured at 45.2  $k\Omega \cdot cm^2$  for 304LB and drops to 16.1  $k\Omega \cdot cm^2$  for 304LB-UNSM post-peening, indicating a decrease in passive film resistance consistent with the polarization properties observed in Figure 10a. The passive film resistance for 304LW measured at 63.6  $k\Omega \cdot cm^2$ , while for 304LW-UNSM after peening, it was 55.1  $k\Omega \cdot cm^2$ , showing a modest increase compared to 304LW, aligning with the behavior in Figure 10b. The welded metal's uneven surface due to welding is shown in Figure 12; it is believed to have been somewhat normalized by peening. Notably, the corrosion resistance reduction due to overlapping is not significant in the welded metal, unlike in the base metal.

Figure 12 depicts the microstructure of a 304L stainless steel surface observed after UNSM treatment. Figure 12a reveals the austenitic microstructure of the base metal; post-UNSM treatment, finely spaced valleys have formed [23]. Figure 12b illustrates the 304L HAZ microstructure, where grains in the fusion line area have coarsened due to thermal effects during welding; the surface post-UNSM exhibits few overlapping areas and fine valleys. Figure 12c displays the microstructure of a 304L weldment, presenting a mixed phase with the formation of  $\delta$ -ferrite in the form of vermicular ferrite (VF) [2,40]. Following UNSM, fewer overlapping areas and a more uniform, flat structure are evident.



**Figure 11.** Effect of UNSM on the EIS of the 304L stainless steel surface in de-aerated 1% NaCl at 30 °C; (a) Nyquist plot, (b) Bode plot, and (c) Polarization resistance.

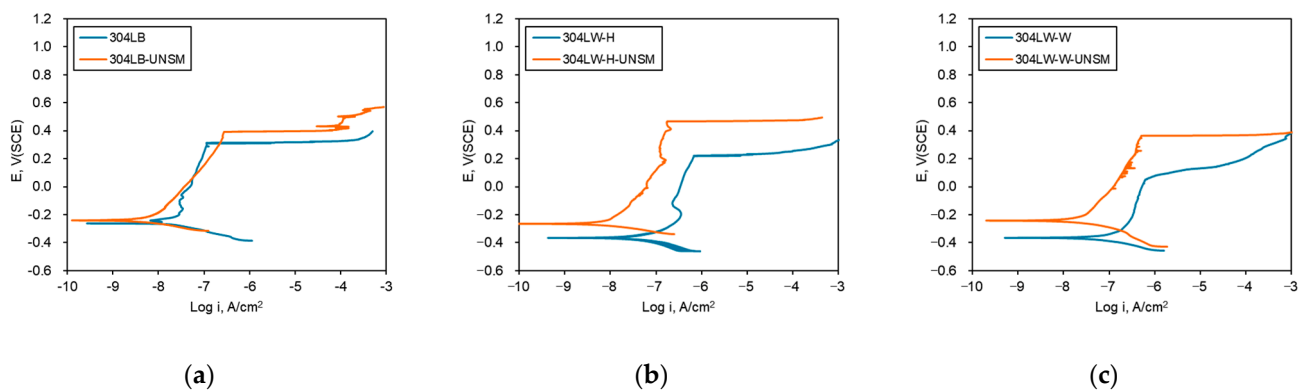


**Figure 12.** Optical microstructure of 304L stainless steel surface post-USNM (OM, ×200, 10% oxalic acid); (a) 304LB (base metal), (b) 304LW-H (HAZ), and (c) 304LW-W (welded metal).

**3.3. Impact of UNSM on the Corrosion Properties and Microstructure of the Cross-Section of 304L Stainless Steel**

Figure 13 illustrates the polarization curves (de-aerated 1% NaCl at 30 °C) of the cross-section of the base metal and welded metal of 304L stainless steel with and without UNSM. Figure 13a shows the polarization curve of 304LB, noting a pitting potential of 287 mV (SCE); the pitting potential of 304LB-UNSM is 391 mV (SCE), indicating a marginal increase in pitting potential after peening. The passive current density at 0 mV (SCE) remains relatively unchanged. Figure 13b presents the polarization curves for the HAZ, where the pitting potential was 220 mV (SCE) for 304LW-H and 469 mV (SCE) for 304LW-H-UNSM, showing enhanced pitting resistance post-peening. The passive current density at 0 mV

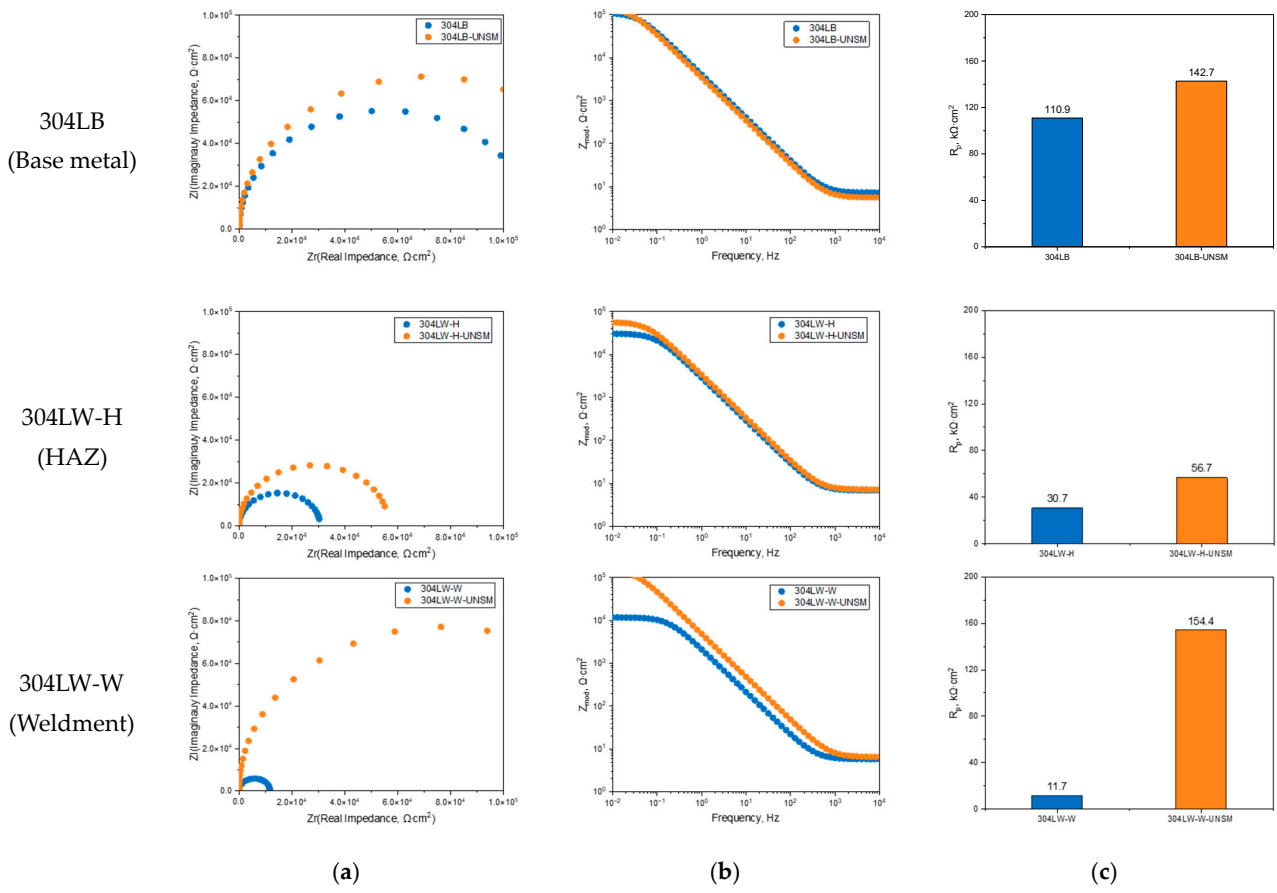
(SCE) is lower for 304W-H-UNSM, suggesting improved corrosion resistance with peening. Figure 13c reveals the polarization curves of the welded metal, where the pitting potential was 53 mV (SCE) for 304LW-W and 366 mV (SCE) for 304LW-W-UNSM, indicating an increase in the pitting potential after peening. The passive current density at 0 mV (SCE) is lower for 304W-W-UNSM, demonstrating enhanced corrosion resistance with peening. The UNSM reduces the interatomic distance in the areas because it generates compressive residual stress in the cross-section, as shown below in microstructure image. As a result, the passive film becomes robust and stronger, increasing its corrosion resistance [2,26].



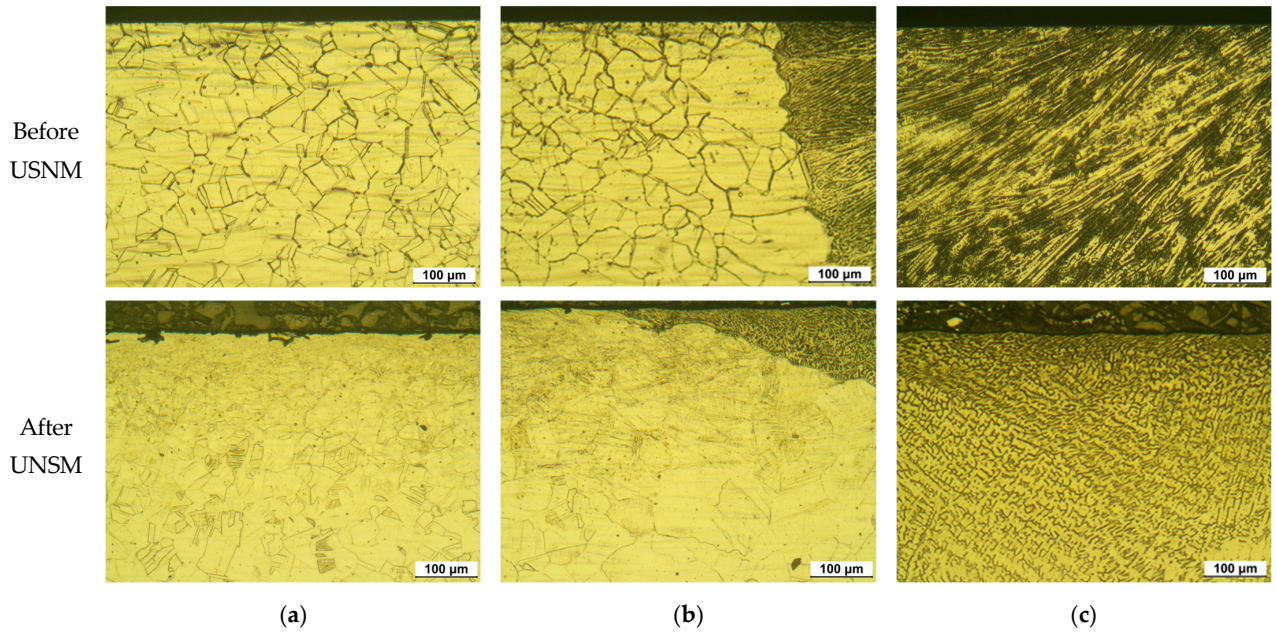
**Figure 13.** Effect of UNSM on the polarization behavior of the cross-section of 304L stainless steel in de-aerated 1% NaCl at 30 °C at a scan rate of 0.33 mV/s; (a) 304LB (Base metal), (b) 304LW-H (HAZ), and (c) 304LW-W (Welded metal).

Figure 14 displays the results of the EIS evaluation on the cross-section of 304L stainless steel following the UNSM treatment. The resistance values of the passive films indicate that the base material 304LB has a resistance of 110.9  $\text{k}\Omega\cdot\text{cm}^2$ , while 304LB-UNSM shows a resistance of 142.7  $\text{k}\Omega\cdot\text{cm}^2$ , demonstrating a modest increase in passive film resistance due to peening, aligning with the polarization properties depicted in Figure 13a. For the HAZ, the resistance of the passive film is 30.7  $\text{k}\Omega\cdot\text{cm}^2$  for 304LW-H and 56.7  $\text{k}\Omega\cdot\text{cm}^2$  for 304LW-H-UNSM, consistent with the increased resistance after UNSM and the improved polarization properties shown in Figure 13b. The welded metal's passive film resistance is 11.7  $\text{k}\Omega\cdot\text{cm}^2$  for 304LW-W and 154.4  $\text{k}\Omega\cdot\text{cm}^2$  for 304LW-W-UNSM, reflecting a substantial increase post-peening and enhanced polarization properties, as seen in Figure 13c. After the UNSM treatment, the outermost regions of the cross-section are refined, forming a robust passivation layer due to compressive residual stresses, thus enhancing the resistance of the film [2].

Figure 15 presents an image of a cross-section of the 304L stainless steel after UNSM treatment (OM,  $\times 200$ , 10% oxalic acid). Figure 15a illustrates the austenitic microstructure in the base metal area where, post-peening, very fine grains are visible within the 30–50  $\mu\text{m}$  outermost section of the cross section. Figure 15b depicts the microstructure of the HAZ, coarsened along the fusion line due to thermal effects during welding; after UNSM treatment, this outermost area exhibits fine grains due to deformation. Figure 15c reveals the microstructure of the welded metal, characterized by a Columnar Dendrite (CD) type; post-UNSM  $\delta$ -ferrite shows a mixed texture of vermicular ferrite (VF) and lathy ferrite (LF), with the outermost regions being finely grained [2,40].



**Figure 14.** Effect of UNSM on the EIS of the 304L stainless steel cross-section in de-aerated 1% NaCl at 30 °C; (a) Nyquist plot, (b) Bode plot, and (c) Polarization resistance.



**Figure 15.** Optical microstructure of the cross-section of 304LW after UNSM (OM, ×200, 10% oxalic acid); (a) 304LB (Base metal), (b) 304LW-H (HAZ), and (c) 304LW-W (Welded metal).

### 3.4. Effect of UNSM on the Residual Stress and SCC of 304L Stainless Steel

Figure 16 illustrates the residual stresses in the base metal and weldments (HAZ and welded metal) of 304L stainless steel following UNSM treatment, with measurements conducted using the hole-drilling method, as reported in the literature [6]. Figure 16a details the residual stresses induced by UNSM along the X-axis, and Figure 16b displays those along the Y-axis. Both the base metal and welded metal (HAZ and weldment) exhibit compressive residual stresses on the X and Y axes up to a depth of 1 mm from the surface, with these stresses diminishing as the depth increases. The compressive residual stress in the base metal and weldment gradually decreases from the surface to the 1 mm area, whereas the HAZ displays variations in the reduction of compressive residual stress due to microstructural transformations caused by the thermal effects of welding [2,41]. Conversely, the non-peened base metal, HAZ, and weldment exhibit residual tensile stresses that diminish with increasing depth from the surface.

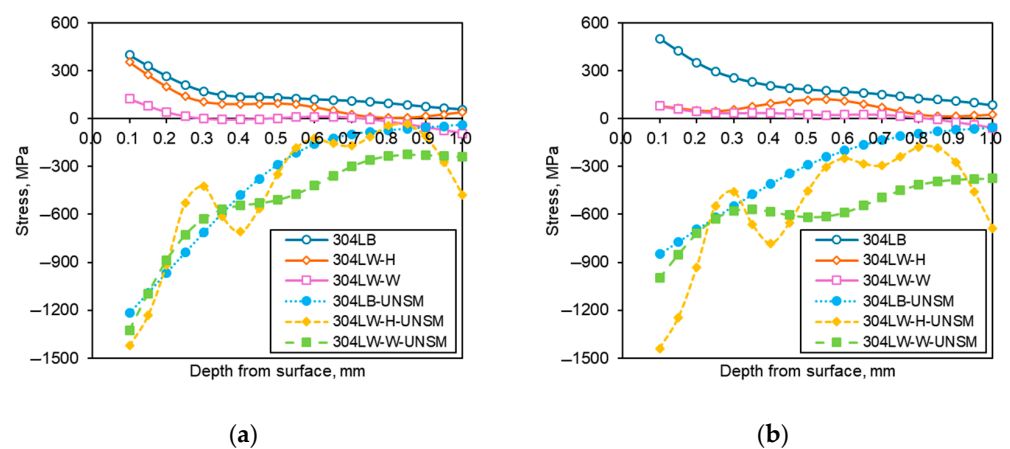


Figure 16. Residual stress in welds of 304L stainless steel post-UNSM; (a) X-axis and (b) Y-axis.

Figure 17 depicts the relationship between crack time and residual stress for 304L stainless steel treated with UNSM. Figure 17a demonstrates the correlation between the base material’s residual stress and crack time, revealing that tensile residual stress leads to a crack time of 3 h, which extends to 9 h when compressive residual stress is applied following UNSM treatment. Figure 17b compares the residual stress and crack time in the weld, indicating that 304LW-H with tensile residual stress exhibits a crack time of 3 h, which increases to 9 h for 304LW-H-UNSM under compressive residual stress post-UNSM. The imposition of compressive residual stresses by UNSM enhances corrosion resistance, thereby prolonging the time to crack [4,19,42,43].

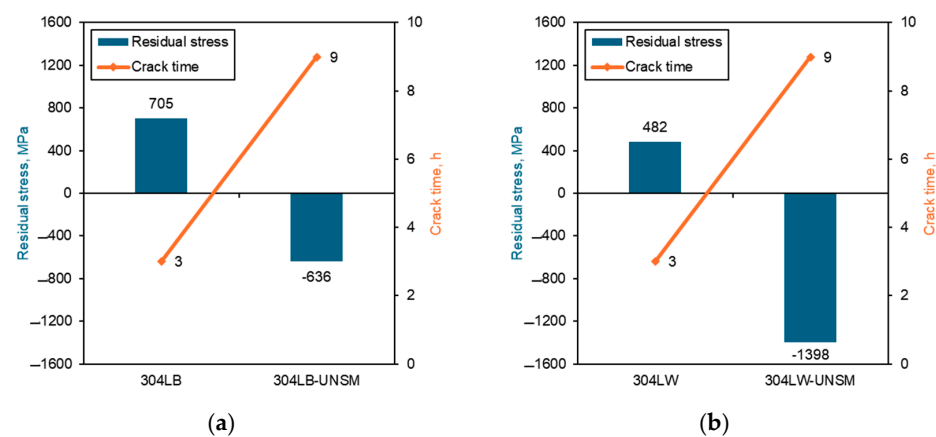


Figure 17. Impact of UNSM on Residual Stress and Crack Time in 304L Stainless Steel; (a) 304LB (Base metal) and (b) 304LW (Welded metal).

#### 4. Discussion

UNSM is a technology used for surface modification by inducing plastic deformation and refined grains to enhance the mechanical properties and surface durability of 304L stainless steel. It generates a refined layer on the steel surface to prevent fatigue and stress corrosion-induced cracking and defects [19]. The plastic deformation and refined grains not only improve the corrosion, wear, and fatigue resistance but also bolster the robustness and reliability of passive films, thereby enhancing overall corrosion resistance [19].

Figure 18 shows a typical DL-EPR test graph and IGC results. The DL-EPR test was measured by anodic (forward) scan to +400 mV (SCE) and then a backward scan to the corrosion potential for reactivation. The corrosion rate was obtained by immersion in HNO<sub>3</sub> solution (boiling point) every 3 h and measuring the weight loss according to the modified ASTM A262 Pr. C. The corrosion rate was obtained by repeating the tests five times and averaging to calculate the IGC rate.

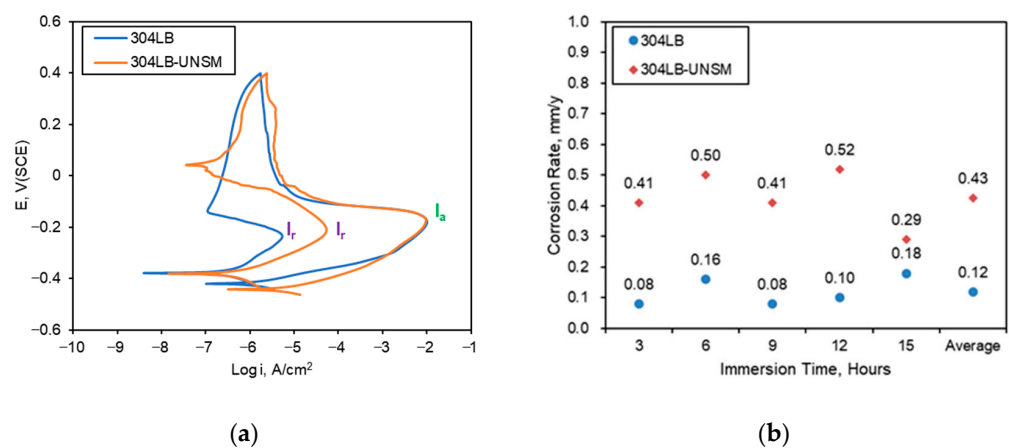


Figure 18. (a) Typical DL-EPR test graph and (b) IGC results.

Table 5 summarizes the corrosion properties of 304L base metal, HAZ, and weldment after UNSM, highlighting the differences between the surface and cross-section and demonstrating the correlation between the crack propagation rate and corrosion properties [2,19].

Table 5. The corrosion properties of 304L base and welded metals upon UNSM treatment.

Peening Condition		$E_p, V (SCE)$ of Surface	$E_p, V (SCE)$ of Cross-Section	DOS, $I_r/I_a$	IGC Rate mm/year
Non-peened	Base Metal	0.935	0.287	0.00003	0.12
	HAZ	−0.040	0.220	0.00095	0.20
	Weldment		0.053	0.00104	
UNSM	Base Metal	−0.056	0.391	0.00550	0.43
	HAZ	−0.002	0.469	0.00351	0.13
	Weldment		0.366	0.00180	

Table 6 presents the correlation between the corrosion properties and crack propagation rate of 304L base metal and welded metal by peening [4]. In Table 6, the determination coefficient ( $R^2$ ) quantifies how the regression model accounts for data variability, while the correlation coefficient ( $R$ ) measures the strength and direction of the linear relationship between two variables. Further, the F-value assesses the significance of the model's explanations, and the  $p$ -value, being less than 0.05, indicates the model's significance; values greater than 0.05 suggest it is not significant.

- (1) The surface pitting potential and crack propagation rate exhibited a positive slope. Typically, higher  $E_p$  enhances the pitting resistance; yet, the crack growth rate also escalated with the increase in  $E_p$  induced by UNSM. The correlation between these two parameters is weak, indicating that high  $E_p$  on the surface compromises SCC resistance, thus suggesting that UNSM-induced  $E_p$  is not effective against SCC.
- (2) The cross-section analysis of the pitting potential and crack propagation rate revealed a negative slope. The crack growth rate decreases as the pitting potential, enhanced by UNSM, increases, improving pitting resistance and effectively suppressing crack growth. Furthermore, the correlation coefficient ranges from  $-0.8861$  to  $-0.9016$  and the coefficient of determination from  $0.7852$  to  $0.8130$ , indicating a strong correlation between the variables.
- (3) The relationship between DOS and crack propagation rate is negatively sloped. Generally, as DOS decreases, the corrosion resistance improves, but the crack growth rate increases. The low coefficients of determination and correlation imply a weak relationship between these variables, suggesting that DOS induced by UNSM is ineffective in resisting SCC.
- (4) The relationship between intergranular corrosion rate and crack propagation rate was negative. Decreasing the intergranular corrosion rate enhances the corrosion resistance; yet, the crack growth rate increases as the intergranular corrosion rate declines due to UNSM. These two parameters exhibit a low coefficient of determination and correlation, and the intergranular corrosion rate adversely affects SCC; thus, it is not an effective parameter for enhancing SCC resistance.

**Table 6.** Correlation of corrosion properties and crack propagation rate in 304L base and welded metals after peening [4].

Corrosion Properties Crack Propagation		Trend Equation	Determination Coefficient, $R^2$	Correlation Coefficient, $R$	F-Value	$p$ -Value
$E_p$ (Surface)	versus Total Crack propagation rate	$y = 0.11x + 1.08$	0.0121	0.1101	0.0491	0.8355
	versus Net Crack propagation rate	$y = 0.66x + 1.72$	0.0500	0.2236	0.2105	0.6702
$E_p$ (Cross- section)	versus Total Crack propagation rate	$y = -2.35x + 1.79$	0.8130	$-0.9016$	0.5624	0.7662
	versus Net crack propagation rate	$y = -7.03x + 3.89$	0.7852	$-0.8861$	14.6173	0.0187
DOS	versus Total crack propagation rate	$y = -120.86x + 1.35$	0.4043	$-0.6359$	2.7150	0.1748
	versus Net crack propagation rate	$y = -65.46x + 2.71$	0.1026	$-0.3203$	0.4572	0.5360
IGC rate	versus Total crack propagation rate	$y = -0.62x + 1.21$	0.0602	$-0.2453$	1.7412	0.7547
	versus Net crack propagation rate	$y = -3.03x + 2.42$	0.1420	$-0.3768$	0.3309	0.6232

Figure 19 illustrates the relationship between residual stress and crack propagation rate in 304L stainless steel base metal and welded metal. Figure 19a depicts how an increase in compressive residual stress reduces the total crack rate, whereas an increase in tensile residual stress elevates it. Figure 19b demonstrates similar findings in the correlation between residual stress and the net crack propagation rate. Compressive residual stress induced by UNSM enhances the pitting resistance, subsequently reducing the crack propagation rate and increasing the SCC resistance [6]. Moreover, the compressive residual stress from UNSM strongly correlates with corrosion resistance, crack initiation time, and crack propagation rate, influencing SCC properties.

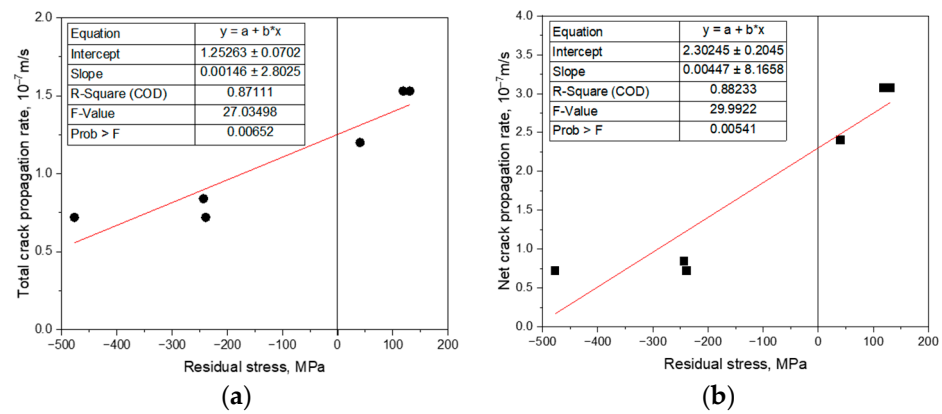


**Figure 19.** Relationship between the crack propagation and residual stress; (a) Total crack propagation rate and (b) Net crack propagation rate.

The effect of UNSM is to convert the tensile residual stress to compressive residual stress, substantially improving SCC resistance. Nonetheless, this improvement in SCC resistance stems not only from compressive residual stress but also from the plastically altered microstructure due to peening, which plays a crucial role in delaying SCC development.

Figure 20 displays a schematic of crack initiation and propagation in 304L stainless steel due to UNSM. Cracks initially develop in areas of concentrated stress, which intensifies at the crack location, promoting further crack growth.

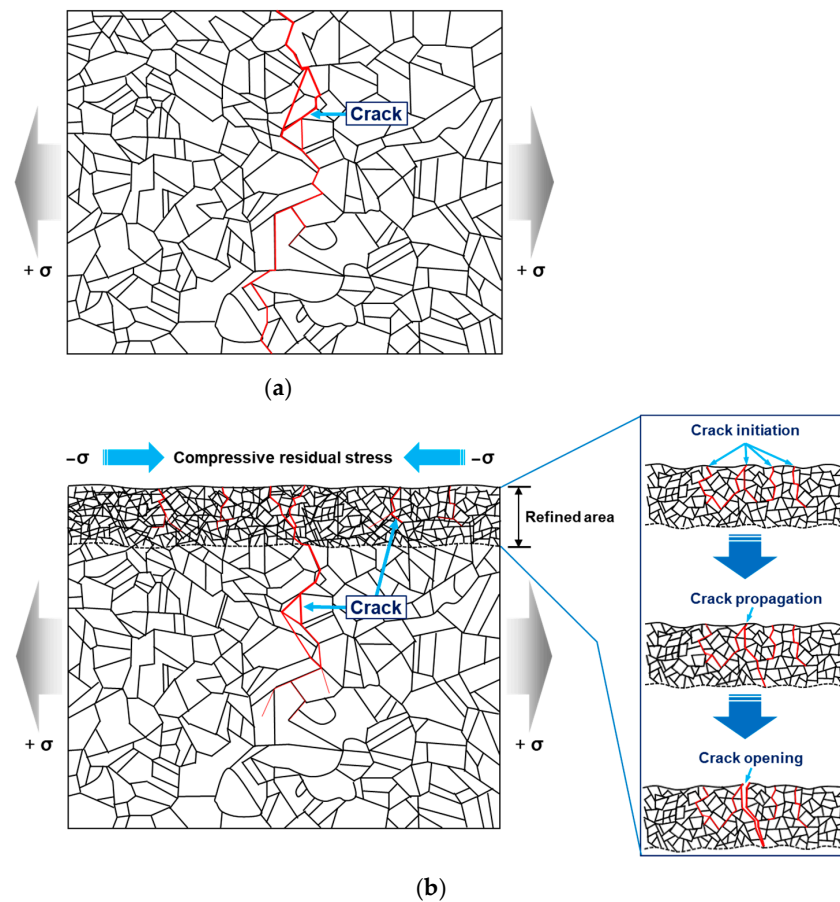


**Figure 20.** Proposed model of crack initiation and propagation of 304L stainless steel upon UNSM treatment; (a) Non-peened, (b) UNSM-treated and crack propagation of the refined area.

As shown in Figure 20a, the non-peened specimen exhibits rapid intergranular and intergranular growth of cracks due to stress concentration. Figure 20b illustrates the plastically deformed microstructure produced by the UNSM-treated specimen, where cracks are generated and propagated through the same mechanism. The refined microstructure created by peening acts to increase crack resistance by allowing multiple cracks to form and grow. In other words, after UNSM treatment, the refined grains from plastic deformation enhance crack resistance as they contribute to multiple crack initiation and propagation, thereby inhibiting crack propagation. The crack initiation and growth in the refined area plastically deformed by UNSM follow the process described below. In the crack initiation phase, multiple cracks initially form in the microscopically plastically deformed grains from the UNSM. During the crack growth phase, multiple cracks expand along fine grains. The cracks extend past the microscopic grain boundaries into the existing tissue, which slows the cracks' growth as they traverse multiple grain boundaries. Several cracks originating within the microscopic grains expand and merge into the existing tissue, with the merged cracks following the same growth mechanism as the tissue unaffected by the UNSM. At this point, the grain opens due to multiple cracks emanating from the fine grain, and the crack spacing increases.

## 5. Conclusions

In this study, the 304L stainless steel base metal and welded metal were treated with UNSM to enhance the SCC properties. We investigated the correlation between microstructure, corrosion properties, and compressive residual stresses on SCC properties through peening treatment, thereby deriving the following conclusions:

- (1) UNSM employs plastic deformation on 304L stainless steel to develop a refined microstructure and robust passivation film, thereby improving the corrosion resistance of the cross-section even though its resistance on the surface was reduced by UNSM. UNSM treatment leads to grain refinement across the cross-section and a tougher surface while reducing crack growth and propagation rates, influencing SCC properties. Conversely, the grain boundary sensitization and the intergranular corrosion rate following peening have a negligible impact on SCC properties.
- (2) SCC is not strongly correlated with initial crack initiation due to pitting and surface defects, and the outermost areas of the cross-section undergo plastic deformation from the peening treatment, impacting the crack properties. Crack growth is associated with the crack mode, and UNSM influences SCC properties through grain refinement. The compressive residual stress induced by UNSM is closely related to the timing of crack initiation and the rate of crack propagation as it facilitates grain refinement, enhances corrosion resistance, and improves SCC properties.

**Author Contributions:** Conceptualization, H.C. and Y.-R.Y.; methodology, H.C.; validation, H.C. and Y.-R.Y.; formal analysis, Y.-S.K.; investigation, H.C.; resources, Y.-R.Y.; data curation, H.C. and Y.-R.Y.; writing—original draft preparation, H.C. and Y.-R.Y.; writing—review and editing, Y.-S.K.; visualization, H.C.; supervision, Y.-S.K.; project administration, Y.-R.Y. and Y.-S.K.; funding acquisition, Y.-S.K. All authors have read and agreed to the published version of the manuscript.

**Funding:** This research was supported by a grant from the 2023–2024 research funds of the Andong National University.

**Data Availability Statement:** The original contributions presented in the study are included in the article, further inquiries can be directed to the corresponding author.

**Conflicts of Interest:** The authors declare no conflicts of interest.

## References

1. John, M.; Ralls, A.M.; Misra, M.; Menezes, P.L. Effect of ultrasonic impact peening on stress corrosion cracking resistance of austenitic stainless-steel welds for nuclear canister applications. *J. Nucl. Mater.* **2023**, *584*, 154590. [[CrossRef](#)]
2. Cho, H.H.; Yoo, Y.R.; Kim, Y.S. Effect of Ultrasonic Shot Peening on Microstructure and Corrosion Properties of GTA-Welded 304L Stainless Steel. *Crystals* **2024**, *14*, 531. [[CrossRef](#)]
3. Ahn, T.; Oberson, G.; DePaula, S. Chloride-Induced Stress Corrosion Cracking of Austenitic Stainless Steel Used for Dry Storage of Spent Nuclear Fuel. *ECS Trans.* **2013**, *50*, 211–226. [[CrossRef](#)]
4. Yoo, Y.R.; Choi, S.H.; Kim, Y.S. Effect of Laser Shock Peening on the Stress Corrosion Cracking of 304L Stainless Steel. *Metals* **2023**, *13*, 516. [[CrossRef](#)]
5. King, F. Container Materials for the Storage and Disposal of Nuclear Waste. *J. Sci. Eng.* **2013**, *69*, 986–1011. [[CrossRef](#)]
6. Cho, H.H.; Yoo, Y.R.; Kim, Y.S. Improvement of Chloride Induced Stress Corrosion Cracking Resistance of Welded 304L Stainless Steel by Ultrasonic Shot Peening. *Corros. Sci. Technol.* **2024**, *23*, 266–277. [[CrossRef](#)]
7. Wang, T.; Yu, J.; Dong, B. Surface Nano Crystallization Induced by Shot Peening and its Effect on Corrosion Resistance of 1Cr18Ni9Ti Stainless Steel. *Surf. Coat. Technol.* **2006**, *200*, 4777–4781. [[CrossRef](#)]
8. Huang, H.; Niu, J.; Xing, X.; Lin, Q.; Chen, H.; Qiao, Y. Effects of the Shot Peening Process on Corrosion Resistance of Aluminum Alloy: A Review. *Coatings* **2022**, *12*, 629. [[CrossRef](#)]
9. Lu, J.Z.; Qi, H.; Luo, K.Y.; Luo, M.; Cheng, X.N. Corrosion Behaviour of AISI 304 Stainless Steel Subjected to Massive Laser Shock Peening Impacts with Different Pulse Energies. *Corros. Sci.* **2014**, *80*, 53–59. [[CrossRef](#)]
10. Cao, X.; Wu, J.; Zhong, G.; Wu, J.; Chen, X. Laser Shock Peening: Fundamentals and Mechanisms of Metallic Material Wear Resistance Improvement. *Materials* **2024**, *17*, 909. [[CrossRef](#)]
11. Kim, J.D.; Sano, Y. Laser peening application for PWR power plants. *J. Weld. Join.* **2016**, *34*, 13–18. [[CrossRef](#)]
12. Ming, T.; Peng, Q.; Han, Y.; Zhang, T. Comparison of the effect of water jet cavitation peening on stress corrosion cracking behavior of nickel-based alloy 600 and alloy 182 in high temperature water. *Anti-Corros. Methods Mater.* **2022**, *69*, 651–659. [[CrossRef](#)]
13. Jiang, W.; Luo, Y.; Wang, H.; Wang, B.Y. Effect of Impact Pressure on Reducing the Weld Residual Stress by Water Jet Peening in Repair Weld to 304 Stainless Steel Clad Plate. *J. Press. Vessel Technol.* **2015**, *137*, 031401. [[CrossRef](#)]
14. Fereidooni, B.; Morovvati, M.R.; Sadough-Vanini, S.A. Influence of severe plastic deformation on fatigue life applied by ultrasonic peening in welded pipe 316 Stainless Steel joints in corrosive environment. *Ultrasonics* **2018**, *88*, 137–147. [[CrossRef](#)] [[PubMed](#)]
15. Manchoul, S.; Sghaier, R.B.; Seddik, R.; Fathallah, R. Comparison between conventional shot peening and ultrasonic shot peening. *Mech. Ind.* **2018**, *19*, 603. [[CrossRef](#)]
16. Amini, S.; Kariman, S.A.; Teimouri, R. The effects of ultrasonic peening on chemical corrosion behavior of aluminum 7075. *Int. J. Adv. Manuf. Technol.* **2017**, *91*, 1091–1102. [[CrossRef](#)]
17. Malaki, M.; Ding, H. A Review of Ultrasonic Peening Treatment. *Mater. Des.* **2015**, *87*, 1072–1086. [[CrossRef](#)]
18. Martin, U.; Röss, J.; Bastidas, D.M. Intergranular SCC mechanism of ultrasonic nanocrystalline surface modified AISI 304 SS in H<sub>2</sub>SO<sub>4</sub> solution containing chloride. *Electrochim. Acta* **2022**, *405*, 139622. [[CrossRef](#)]
19. Kishore, A.; John, M.; Ralls, A.M.; Jose, S.A.; Kuruveri, U.B.; Menezes, P.L. Ultrasonic Nanocrystal Surface Modification: Processes, Characterization, Properties, and Applications. *Nanomaterials* **2022**, *12*, 1415. [[CrossRef](#)]
20. Amanov, A. Effect of local treatment temperature of ultrasonic nanocrystalline surface modification on tribological behavior and corrosion resistance of stainless steel 316L produced by selective laser melting. *Surf. Coat. Technol.* **2020**, *398*, 126080. [[CrossRef](#)]
21. Kim, M.S.; Park, S.H.; Pyun, Y.S.; Shim, D.S. Optimization of ultrasonic nanocrystal surface modification for surface quality improvement of directed energy deposited stainless steel 316L. *J. Mater. Res. Technol.* **2020**, *9*, 15102–15122. [[CrossRef](#)]
22. Wang, Q.; Li, Y.; Lu, Z.; Zhang, Y.; Zou, Y. Effects of Ultrasonic Nanocrystal Surface Modification on Mechanical and Corrosion Behavior of LZ91 Mg-Li Alloy. *Mater. Trans.* **2020**, *61*, 1258–1264. [[CrossRef](#)]
23. Kim, K.T.; Kim, Y.S. The Effect of the Static Load in the UNSM Process on the Corrosion Properties of Alloy 600. *Materials* **2019**, *12*, 3165. [[CrossRef](#)]
24. Cao, X.J.; Pyoun, Y.S.; Murakami, R. Fatigue properties of a S45C steel subjected to ultrasonic nanocrystal surface modification. *Appl. Surf. Sci.* **2010**, *256*, 6297–6303. [[CrossRef](#)]
25. Zhao, W.; Liu, D.; Chiang, R.; Qin, H.; Zhang, X.; Zhang, H.; Liu, J.; Ren, Z.; Zhang, R.; Doll, G.L.; et al. Effects of ultrasonic nanocrystal surface modification on the surface integrity, microstructure, and wear resistance of 300M martensitic ultra-high strength steel. *J. Mater. Process. Technol.* **2020**, *285*, 116767. [[CrossRef](#)]
26. Karthik, D.; Swaroop, S. Effect of laser peening on electrochemical properties of titanium stabilized 321 steel. *Mater. Chem. Phys.* **2017**, *193*, 147–155. [[CrossRef](#)]
27. Ma, C.; Andani, M.T.; Qin, H.; Moghaddam, N.S.; Ibrahim, H.; Jahadakbar, A.; Amerinatanzi, A.; Ren, Z.; Zhang, H.; Doll, G.L.; et al. Improving surface finish and wear resistance of additive manufactured nickel-titanium by ultrasonic nanocrystal surface modification. *J. Mater. Process. Technol.* **2017**, *249*, 433–440. [[CrossRef](#)]
28. Efe, Y.; Karademir, I.; Husem, F.; Maleki, E.; Karimbaev, R.; Amanov, A.; Unal, O. Enhancement in microstructural and mechanical performance of AA7075 aluminum alloy via severe shot peening and ultrasonic nanocrystal surface modification. *Appl. Surf. Sci.* **2020**, *528*, 146922. [[CrossRef](#)]

29. Amanov, A.; Karimbaev, R.; Maleki, E.; Unal, O.; Pyun, Y.S.; Amanov, T. Effect of combined shot peening and ultrasonic nanocrystal surface modification processes on the fatigue performance of AISI 304. *Surf. Coat. Technol.* **2019**, *358*, 695–705. [[CrossRef](#)]
30. Niu, W.; Li, Z.; Ernst, F.; Ren, Z.; Ye, C.; Lillard, R.S. Stress-Corrosion Cracking of Surface-Engineered Alloys in Simulated Boiling-Water-Reactor Environment. *Corrosion* **2018**, *74*, 635–653. [[CrossRef](#)]
31. Lee, J.H.; Kim, K.T.; Pyoun, Y.S.; Kim, Y.S. Intergranular Corrosion Mechanism of Slightly-Sensitized and UNSM-treated 316L Stainless Steel. *Corros. Sci. Technol.* **2016**, *15*, 226–236. [[CrossRef](#)]
32. Ling, X.; Ma, G. Effect of Ultrasonic Impact Treatment on the Stress Corrosion Cracking of 304 Stainless Steel Welded Joints. *J. Press. Vessel Technol.* **2009**, *131*, 051502. [[CrossRef](#)]
33. *ASTM G30-2003*; Standard Practice for Making and Using U-Bend Stress-Corrosion Test Specimens. ASTM International: West Conshohocken, PA, USA, 2003.
34. *ASTM G58-2015*; Standard Practice for Preparation of Stress-Corrosion Test Specimens for Weldments. ASTM International: West Conshohocken, PA, USA, 2015.
35. *ASTM G36-2000*; Standard Practice for Evaluating Stress-Corrosion-Cracking Resistance of Metals and Alloys in a Boiling Magnesium Chloride Solution. ASTM International: West Conshohocken, PA, USA, 2000.
36. *ASTM G108-2004*; Standard Test Method for Electrochemical Reactivation (EPR) for Detecting Sensitization of AISI Type 304 and 304L Stainless Steels. ASTM International: West Conshohocken, PA, USA, 2004.
37. Turnbull, A.; Mingard, K.; Lord, J.D.; Roebuck, B.; Tice, D.R.; Mottershead, K.J.; Fairweather, N.D.; Bradbury, A.K. Sensitivity of stress corrosion cracking of stainless steel to surface machining and grinding procedure. *Corros. Sci.* **2011**, *53*, 3398–3415. [[CrossRef](#)]
38. Spencer, D.T.; Edwards, M.R.; Wenman, M.R.; Tsitsios, C.; Scatigno, G.G.; Chard-Tuckey, P.R. The initiation and propagation of chloride-induced transgranular stress-corrosion cracking (TGSCC) of 304L austenitic stainless steel under atmospheric conditions. *Corros. Sci.* **2014**, *88*, 76–88. [[CrossRef](#)]
39. *ASTMG3-2004*; Standard Practice for Conventions Applicable to Electrochemical Measurements in Corrosion Testing. ASTM International: West Conshohocken, PA, USA, 2004.
40. Kim, S.C.; Hyun, J.H.; Shin, T.W.; Koh, J.H. A Study of Characteristics on the Dissimilar Metals (ASTM Type 316L—Carbon Steel: ASTM A516-70) Welds Made with FCA Multiple Layer Welding. *J. Weld. Join.* **2016**, *34*, 69–76. [[CrossRef](#)]
41. Kawano, S.; Kawagishi, A.; Suezono, N.; Ueno, K.; Okuda, K.; Obata, M.; Kameyama, I.; Watanabe, Y. Development of Ultrasonic Shot Peening Technique for Reactor Components to Improve Structural Integrity Against Stress Corrosion Cracking. In Proceedings of the 17th International Conference on Nuclear Engineering, Brussels, Belgium, 12–16 July 2009.
42. Lu, J.Z.; Luo, K.Y.; Yang, D.K.; Cheng, X.N.; Hu, J.L.; Dai, F.Z.; Qi, H.; Zhang, L.; Zhong, J.S.; Wang, Q.W.; et al. Effects of laser peening on stress corrosion cracking (SCC) of ANSI 304 austenitic stainless steel. *Corros. Sci.* **2012**, *60*, 145–152. [[CrossRef](#)]
43. Yoo, Y.R.; Choi, S.H.; Kim, Y.S. Effect of Laser Peening on the Corrosion Properties of 304L Stainless Steel. *Materials* **2023**, *16*, 804. [[CrossRef](#)]

**Disclaimer/Publisher’s Note:** The statements, opinions and data contained in all publications are solely those of the individual author(s) and contributor(s) and not of MDPI and/or the editor(s). MDPI and/or the editor(s) disclaim responsibility for any injury to people or property resulting from any ideas, methods, instructions or products referred to in the content.